OXFORD

BIOLOGY Methods & Protocols

Biology Methods and Protocols, 2025, **10(1),** bpaf019

https://doi.org/10.1093/biomethods/bpaf019
Advance Access Publication Date: 11 March 2025
Methods Article

Flow cytometric procedures for deep characterization of nanoparticles

Valentina Tirelli[1,*,‡], Felicia Grasso[2,‡], Valeria Barreca[3], Deborah Polignano[3], Alessandra Gallinaro[3], Andrea Cara[3], Massimo Sargiacomo[3], Maria Luisa Fiani[3] Massimo Sanchez[1,*]

[1]Core Facilities, Istituto Superiore di Sanità, viale Regina Elena 299, 00161, Roma, Italy
[2]Department of Infectious Diseases, Istituto Superiore di Sanità, viale Regina Elena 299, 00161, Roma, Italy
[3]National Centre of Global Health, Istituto Superiore di Sanità, viale Regina Elena 299, 00161, Rome, Italy

*Corresponding authors. Valentina Tirelli, Core Facilities, Istituto Superiore di Sanità, viale Regina Elena 299, 00161, Rome, Italy. E-mail: valentina.tirelli@iss.it; Massimo Sanchez, Core Facilities, Istituto Superiore di Sanità, viale Regina Elena 299, 00161, Rome, Italy. E-mail: massimo.sanchez@iss.it

‡Contributed equally to this work.

Abstract

In recent years, there has been a notable increasing interest surrounding the identification and quantification of nano-sized particles, including extracellular vesicles (EVs) and viruses. The challenge posed by the nano-sized dimension of these particles makes precise examination a significant undertaking. Among the different techniques for the accurate study of EVs, flow cytometry stands out as the ideal method. It is characterized by high sensitivity, low time consumption, non-destructive sampling, and high throughput. In this article, we propose the optimization of flow cytometry procedures to identify, quantify, and purify EVs and virus-like particles. The protocol aims to reduce artefacts and errors in nano-sized particles counting, overall caused by the swarming effect. Different threshold strategies were compared to ensure result specificity. Additionally, the critical parameters to consider when using conventional flow cytometry outside of the common experimental context of use have also been identified. Finally, fluorescent-EVs sorting protocol was also developed with highly reliable results using a conventional cell sorter.

Graphical abstract

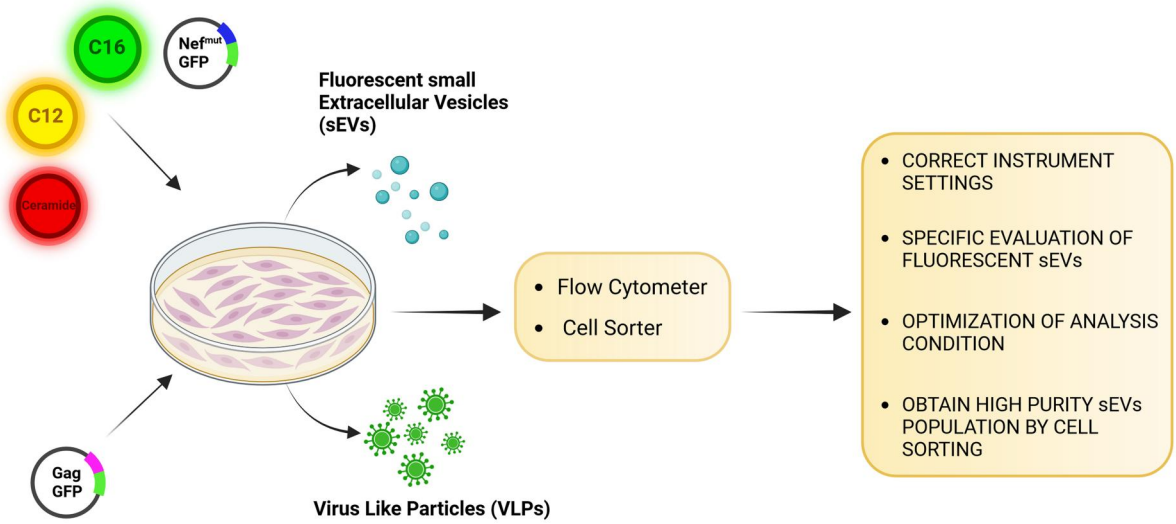

Keywords: Flow Cytometry, extracellular vesicles, EVs

Received: 4 October 2024; **Revised:** 28 February 2025; **Editorial decision:** 3 March 2025; **Accepted:** 6 March 2025

Introduction

The identification of extracellular vesicles (EVs) has received increasing attention in recent years. EVs are a heterogeneous population exhibiting variability in size and shape and encompassing exosomes, microvesicles, and apoptotic bodies [1–3].

EVs play roles in both autocrine and paracrine signalling, functioning as mediators of cellular communication, participating in normal physiological processes as well as pathological conditions. These membrane vesicles carry proteins, nucleic acids, and bioactive lipids resembling the cell of origin [4]. Once released within the extracellular space and entering the circulation, EVs may transfer their cargo to neighbouring or distant cells inducing phenotypical and functional changes [5, 6]. The unique characteristics of EVs identify them as non-invasive diagnostic biomarkers for the diagnosis and prognosis of various diseases, offering potential contributions to the development of next-generation therapeutic nano-carriers [7].

Among nano-carriers, virus-like particles (VLPs) also represent an attractive platform for the delivery of proteins or drugs in both vaccination and therapeutic strategies, combining ease of production, immunogenicity, and high biosafety profile. Indeed, VLPs are small particles (20–200 nm) able to self-assemble, incorporating viral structural proteins and mimicking the shape, size and antigenic display of the parental virus. Importantly, since VLPs lack the genetic material, they are non-infectious and non-replicating, avoiding the risk of active infection in exposed individuals. Furthermore, VLPs can display on their surface high density of homologous or heterologous membrane-tethered glycoprotein, inducing strong cellular and humoral immune responses [8].

In this context, there is a critical need for a tool capable of distinguishing variations in the number of nanoparticles (NPs) from changes in molecular composition and providing multi-parametric analysis at the level of individual NPs.

Despite the development of various standard methods for isolating EVs from different sources, the accurate characterization and quantification of these vesicles have prompted the exploration of several technologies. Nanoparticle tracking analysis (NTA), tunable resistive pulse sensing (TRPS), dynamic light scattering, electron microscopy (EM), and flow cytometry (FCM) are among the technologies employed, each exhibiting its own set of advantages and disadvantages [9–13].

Although FCM is an ideal technique for high throughput, multi-parametric characterization of single events, conventional FCM encounters challenges in detecting particles below the 200 nm, making precise identification of sub-micron particles difficult [14, 15].

FCM is a technique for studying single-cell suspensions that is widely used in both clinical and experimental research. Its quick analysis of many events makes it a valuable tool for obtaining precise quantitative and qualitative data on samples. Employing blue laser excitation (488 nm), FCM evaluates cell morphology through forward scatter (FSC) and side scatter (SSC) signals, measuring cell size and cellular complexity, respectively. Although classically applied in immunology, haematology, oncology, and clinical biology or diagnostics, FCM is increasingly finding applications in non-conventional fields such as microbiology, industry, and the environment [16–19]. Furthermore, due to its high potential, FCM applications are emerging in the identification of submicron sized EVs [20, 21].

Most conventional flow cytometers are designed to detect particles larger than 1 μm. However, for smaller particles, including most viruses (which range in size from 30 to 350 nm) and EVs, there is a necessity to optimize and implement analysis and acquisition protocols in order to achieve sufficient sensitivity [22, 23].

Several strategies have been employed to enhance the sensitivity of FCM. First, fluorescence is essential for the detection of particles smaller than 200 nm in size [21, 23, 24]. Fluorescence enables the reduction of background noise facilitating the confident identification of the EVs under investigation. Another strategy involves utilizing the 405 nm Violet Side Scatter (V-SSC) signal instead of the classic 488 nm Blue Side Scatter (B-SSC). As described by Zucker *et al.*, V-SSC exhibits a higher separation index than B-SSC and shows a smaller coefficient of variation (CV), thereby enhancing the detection limit of FCM, allowing for the identification of 150 nm polystyrene particles [25, 26].

Although technological advances in the design of new flow cytometers have led to a significant improvement in the size sensitivity, there are still no instruments capable of clearly identifying and quantifying EVs, relying solely on physical or morphological parameters. The main difficulty is represented by the background noise, including optical and electronic noise signals, which can overlap with EVs below 200 nm in size.

Furthermore, considering the extremely small dimensions of the EVs, the swarm effect should not be underestimated. This effect occurs when two or more small particles pass through the laser at the same time and are considered as a single particle, leading to an incorrect evaluation of the number of nanoparticles present in the sample [27, 28].

The goal of our work is to develop specific and sensitive FCM procedures to identify and to quantify nano-sized particles (e.g. viruses and EVs) in biological samples. To achieve this, we will use two different types of well-characterized nano-sized particles: EVs isolated from the supernatant of a melanoma cell line, and lentivirus-based VLPs [14, 29]. Furthermore, the development of the analysis protocol for the correct identification of these particles allowed us to transfer it to cell sorter, enabling the purification of specific EVs.

Materials and methods

Cell culture

Human melanoma cells A375M and human embryonic kidney 293T cells (HEK293T) were cultured in Dulbecco's modified Eagle's medium (DMEM). All media were supplemented with 10% heat-inactivated foetal bovine serum (FBS), 100 units/ml penicillin, 100 μg/ml streptomycin, and 2 mM L-glutamine (complete media). Additional 1% minimum essential medium non-essential amino acids were added to A375M cell media. All media and supplements were from Euroclone.

HEK 293 T Lenti-X human embryonic kidney cells (Clontech, Mountain View, CA, USA), used to VLPs production, were maintained in DMEM (Gibco Life Technologies Italia, Monza, Italy), supplemented with 10% FBS (Corning, Mediatech Inc., Manassas, VA, USA), and 100 units/mL penicillin/streptomycin (Gibco).

Cell lines were grown at 37°C, under 5% CO_2, in humidified incubators and routinely tested for mycoplasma contamination using the Mycoplasma PCR Detection Kit (ABM, #G238). All cell lines are commercially available (ATCC).

Extracellular vesicle labelling and collection

BODIPY™ FL C16 (C16) (4,4-Difluoro-5,7-Dimethyl-4-Bora-3a, 4a-Diaza-s-Indacene-3-Hexadecanoic Acid (ThermoFisher, #D3821) or BODIPY 558/568 C12 (C12) (4,4-Difluoro-5-(2-Thienyl)-4-Bora-

3a, 4a-Diaza-s-Indacene-3-Dodecanoic Acid) (ThermoFisher, #D3835) were complexed with fatty acid-free bovine serum albumin (H-BSA, Sigma, #A8806) as described previously [30]. To isolate EVs, 60%–70% confluent monolayers of A375M cells in exponential growth were incubated with 7 μM C16 or C12 at 37°C for 4 h in medium containing antibiotics and glutamine and supplemented with 0.3% FBS (cell labelling medium). To obtain double labelled C16/C12 EVs, A375M cells were incubated with cell labelling medium containing 7 μM C16 and 7 μM C12 for 4 h. To obtain double labelled C16/Ceramide EVs, A375M cells were incubated with 5 μM BODIPY TR Ceramide (ThermoFisher, # D7540) complexed to BSA for 90 min on ice, washed twice with Hank's balanced salt solution (HBSS, Euroclone) and further incubated with 5 μM C16 in cell labelling medium for 90 min at 37°C. To obtain double labelled Nef^{mut}-GFP/C12 EVs, HEK293T cells were transfected with a plasmid encoding Nef^{mut}-GFP as described in Ferrantelli et al. [24]. Briefly, HEK293T cells were transfected with 1 μg/ml plasmid DNA complexed with 3 μg/ml branched polyethylenimine (Sigma-Aldrich # 408727). After 18 h, cells were washed once in HBSS and incubated with 7 μM C12 in cell labelling medium for 4 h at 37°C. At the end of the incubation with fluorescent lipid, cells were washed twice with HBSS containing 0.1% (w/v) H-BSA to remove excess probe and further incubated for 24 h in complete culture medium. The conditioned medium was either immediately processed for EVs isolation or stored at 4°C for up to one week. Cells were detached from the plates with trypsin/EDTA, and their viability was assessed by Trypan Blue exclusion. Conditioned medium containing fluorescent EVs was serially centrifuged at 2000 *g* for 20 min at 4°C to discard cells and large debris. The supernatant was then centrifuged at 10,000 *g* for 20 min at 4°C to pellet microvesicles and other debris. To isolate EVs, the supernatant from previous centrifugation was ultra-centrifuged 100,000 *g* for 90 min at 4°C and the pellet (100K pellet) was washed in 12 ml of phosphate buffered saline (PBS) and centrifuged again at 100,000 *g*. Pellets were re-suspended in 100–150 μl of PBS. All ultracentrifugation steps will be performed at 4°C using a SW41 Ti rotor (Beckman Coulter, Brea, CA, USA).

VLPs' preparation and collection

To produce Lentivirus-based VLPs, 293 T Lenti-X cells were transiently transfected on 10 cm Petri dishes with 8 μg of pGagGFP plasmid, encoding the codon-optimized Gag protein fused to the green fluorescent protein (GFP) [31], using JetPrime transfection kit (Polyplus Transfection, Illkirch, France). After 48 h, cell culture supernatants were recovered, cleared from cellular debris by low-speed centrifugation, passed through a 0.45 μM pore size filter (Millipore Corporation, Billerica, MA, USA) and concentrated by ultra-centrifugation for 2.5 h at 65,000 × *g* using a 20% sucrose cushion. VLPs were dissolved in 1× phosphate buffered saline (PBS, Gibco) and stored at −80°C until use.

Flow cytometric acquisition of beads, EVs and VLPs

All acquisition experiments were performed using a CytoFLEX LX flow cytometer (Beckman Coulter Life Sciences), equipped with five lasers (355, 405, 488, 561, and 640 nm wavelengths). This instrument allows to set the V-SSC in addition to the standard blue laser SSC (B-SSC). Although PBS seems an obvious choice for a sheath fluid, PBS may increase the formation of calcium phosphate crystals in the fluidics system, which may cause additional background noise, clogging, or loss of laminar flow. Therefore, we used purified water as a sheath fluid. Anyway, scatter and all fluorescence parameters were set to log scale. We use two different fluorescent reference beads to fine-tune the instrument: Megamix-Plus FSC with the following diameters: 0.1 μm, 0.3 μm, 0.5 μm, and 0.9 μm and Megamix-Plus SSC with following diameters: 0.16 μm, 0.20 μm, 0.24 μm, and 0.5 μm (BioCytek Marseille, France). The beads were mixed (Megamix-Plus FSC/SSC) and diluted with PBS, following the instructions in the technical datasheet. Beads and all samples (EVs and VLPs) were diluted in PBS. Before starting the acquisition, the instrument underwent a thorough washing protocol. This procedure is crucial for minimizing contaminants and reducing non-specific signals. Acquisition data were analysed by CytExpert v2.3 software.

FCM sorting of EVs

Sorting experiments were performed on MoFlo Astrios-EQ flow cytometer (Beckman Coulter), equipped with four lasers (405, 488, 561, and 640 nm wavelengths) and with a high-sensitivity FSC detector (488ex-FSC). Furthermore, the Astrios-EQ system is provided with inline sheath canister filters of 40 nm pore size. FSC detectors (FSC1 and FSC2) mounted the mask M1 and P1, respectively. Instrument was aligned with Rainbow QC Beads (Spherotech), while the detector settings for nanovesicle detection and fine-tuning adjustments of the alignment were made with Megamix-Plus FSC/SSC beads (BioCytek). The instrument acquisition software was Summit v6.3.1. Analyses were performed with both Summit and FlowJo™ v10.9.0 Softwares.

NTA

EVs secreted by A375M cells, labelled with Bodipy FL C16 and Bodipy C12 together, have been quantified pre- and post-sorting by NTA performed with a NanoSight NS300 system (Malvern Instruments, UK). As negative control EVs secreted by the same initial number of unlabelled cells were used. Camera level was set at 16 for all recordings. Camera focus was adjusted to make the particles appear as sharp individual dots. For pre-sorting sample, five 60-second videos were recorded, while for post-sorting sample three 60-seconds videos were recorded with all with a delay of 7 s between each recording at a fixed temperature of 25°C. Analysis was performed with NTA 3.4.4 software. Detection threshold was set at 6 and other settings were kept at default.

Statistical analyses

The results are shown as the means ± standard deviation (SD). The data were evaluated for statistical significance using Student's t-test. Any *P*-value $<.05$ was considered statistically significant.

Results

Threshold settings for detection of fluorescent EVs

We previously described a promising approach for the study of fluorescent EVs [24, 30], where the evaluation of fluorescent EVs using a conventional flow cytometer (Gallios, Beckman Coulter) was described. The main strategy was to use their fluorescent emission rather than light-scattering detection, setting the threshold on fluorescence channel. This approach allows the detection of particles regardless of their size.

The evolution of technology led us to transfer this approach to more advanced instruments with enhanced performance, such as the CytoFLEX LX (Beckman Coulter). The initial step involved defining the sensitivity limit of the instrument. Since the CytoFLEX LX is equipped with the violet laser (405 nm

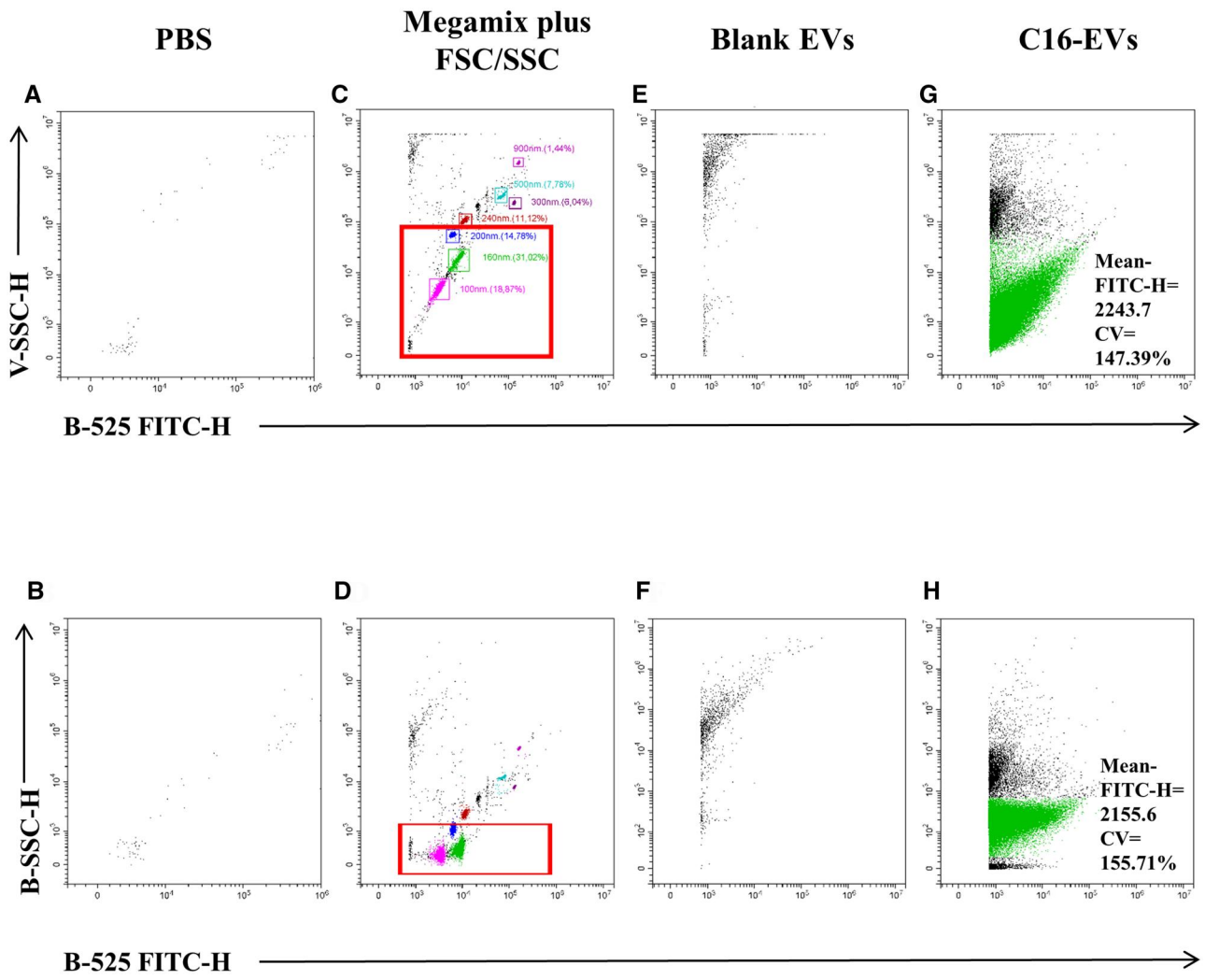

Figure 1. Comparison between V-SSC and B-SSC resolutions for fluorescent EVs detection with threshold applied on FITC fluorescent channel (band pass 525/40). (**A, B**) FCM analysis of 0.22 μm filtered PBS (dot plot of V-SSC-H or BSSC-H versus FITC-H) used to define threshold and gain values. (**C, D**) Megamix Plus FSC/SSC polystyrene beads are used to define the resolution limit of the instrument and to compare the efficiency in separating smallest beads on V-SSC-H compared to the conventional B-SSC-H. Red boxes include beads between 100 and 200 nm in size. (**E, F**) FCM analysis of unstained EVs released by A375M melanoma cell line (blank EVs). (**G, H**) FCM analysis of fluorescent EVs released by A375M melanoma cell line pulsed with the green fluorescent fatty acid, BODIPY^{TM} FL C16 (C16-EVs). Numbers in the plot indicate mean and CV values of C16-EVs visualized by V-SSC-H and B-SSC-H

wavelength), we compared the resolution efficiency in separating small fluorescent beads gathered on V-SSC with the more common B-SSC. Given that FSC is less sensitive to resolving EVs, a mix of two types of green fluorescent beads, Megamix Plus FSC/SSC, with dimensions between 100 and 900 nm, was employed as a reference to determine the size sensitivity limit of the cytometer. These reference beads enabled the establishment of both the threshold and gain levels, achieving a good compromise between sensitivity limits and the exclusion of background noise. The visualization of all the fluorescent beads was obtained by modulating the threshold and gain values on the Fluorescein isothiocyanate (FITC) fluorescent channel (band pass 525/40), maintaining the background noise of the PBS barely detectable (<10 events/second), as shown in Fig. 1A and B, both for V-SSC and the B-SSC parameters. As shown in Fig. 1C and D, the threshold set to fluorescence allows all beads to be detected on both V- and B-SSC channels, although the separation of the smallest beads (between 100 and 200 nm) is much more efficient on V-SSC compared to B-SSC (Fig. 1C and D, red boxes). To further demonstrate the better resolution of V-SSC instead of B-SSC, we calculated the resolution index (RI) of different beads. The RI was calculated with respect to the 100 nm microspheres (the smallest) by the formula as follows: $(MFI_{X\ nm\ beads} - MFI_{100\ nm\ beads})/2 \times SD_{100\ nm\ beads}$). Furthermore, RI as well as the CV and mean of the diverse beads are reported in Table 1. The data demonstrate that the V-SSC (Table 1A) exhibits a RI of 9.14 ± 0.5 between the peaks at 160 and 100 nm, compared to the B-SSC (Table 1B) which has a RI of 1.03 ± 0.14 ($P \leq .0001$). The RI of the V-SSC is always higher than that of the B-SSC, even for the resolution between 200 nm versus 100 and 240 nm versus 100 nm ($P \leq .0001$). Furthermore, the CV values of the individual beads are also lower for V-SSC than for BSSC, especially for the window of interest up to 200 nm: the data show how the CVs of the V-SSC are approximately three times narrower than B-SSC (16.5% vs 39.2% for 100 nm beads, 12.6% vs 34% for 160 nm beads, 6.2% vs 17.7% for 200 nm beads).

Then, to identify fluorescent EVs, both threshold and gain values, defined on PBS, were checked using non-fluorescent EVs (blank EVs). As shown in Fig. 1E and F, blank EVs were barely

Table 1. The table summarizes the values of CV, mean, and RI of the beads evaluated by V-SSC-H (A) or B-SSC-H (B), respectively.

(A) V-SSC- H

	100 nm	160 nm	200 nm	240 nm	300 nm	500 nm	900 nm
RI vs 100 nm		9.14 ± 0.5	29.4 ± 1.81	58.79 ± 3.93	136.27 ± 8.88	197.08 ± 12.28	869.52 ± 52.34
CV	16.5% ± 0.01	12.6% ± 0.01	6.2% ± 0.02	7.6% ± 0.02	6.1% ± 0.02	7.2% ± 0.02	6.2% ± 0.01
Mean	5146.4 ± 124.3	20636.0 ± 491.6	54501.0 ± 1510.23	104694.1 ± 3236.1	235937.7 ± 7807.8	338931.9 ± 9961.4	1478054.6 ± 45179.9

(B) B-SSC-H

	100 nm	160 nm	200 nm	240 nm	300 nm	500 nm	900 nm
RI vs 100 nm		1.03 ± 0.14****	5.45 ± 0.70****	12.83 ± 1.67****	47.22 ± 6.45****	74.35 ± 9.63****	267.43 ± 35.17****
CV	39.2% ± 0.06****	34% ± 0.1****	17.7% ± 0.15**	12.4% ± 0.04***	5.5% ± 0.02	7.0% ± 0.02	9.4% ± 0.03****
Mean	227.05 ± 3.3****	406.64 ± 5.2****	1178.73 ± 30.4****	2467.67 ± 74.9****	8479.45 ± 476.2****	13228.1 ± 622.9****	46957.8 ± 1895.1****

The RI was calculated with respect to the 100 nm beads using the formula: $(MFI_{X\ nm\ beads} - MFI_{100nm\ beads})/2*SD_{100nm\ baeds})$. The V-SSC demonstrates enhanced resolution for small-dimension beads as indicated by higher RI and a relatively low CV. Data are expressed as mean ± SD of 11 independent experiments. Significance was calculated by comparing RI, CV, and mean of B-SSC-H vs V-SSCH by paired t-test.
** $P < .01$, *** $P < .001$, **** $P < .0001$.

visualized, although there is an increase in background noise above the region corresponding to the 400–500 nm beads. Fluorescent EVs were purified from the cell culture supernatant of the A375M melanoma cell line pulsed with the green fluorescent fatty acid, BODIPY™ FL C16 (hereinafter as C16, λex 505 nm/λem 512 nm), as described in the Materials and methods section. As shown in Fig. 1G and H, the fluorescence distribution of C16-EVs using both thresholds (V-SSC and B-SSC) are very similar but a better resolution of C16-EVs was confirmed on the V-SSC channel.

An analogous acquisition strategy was applied to EVs secreted by cells pulsed with the orange-red fluorescent fatty acid, BODIPY™ FL C12 (referred to as C12, λex 558/λem 568 nm). In this case, the threshold was applied to the Phycoerythrin (PE) fluorescent channel (band pass 585/42, hereinafter Y-585 PE-H). The dot plots (V-SSC-H versus B-525 FITC-H or Y-585 PE-H) represented in Fig. 2 display events recorded for PBS (Fig. 2A and B) and blank EVs (Fig. 2C and D) when applying the threshold on both FITC (on the left) or PE (on the right) channels. Fig. 2E and H show the events recorded for C16- and C12-EVs respectively, acquired with their respective threshold. As further control, we acquired C16- and C12-EVs by crossing the thresholds (Fig. 2F and G, respectively).

These results demonstrate that thresholds applied to a specific wavelength can efficiently exclude other fluorescence emission associated with EVs during acquisition, and the presence or absence of signal in a specific acquisition protocol is not an artefact.

In conclusion, this approach for instrument setting allows for an easy and specific evaluation of fluorescent EVs in each sample, effectively minimizing background noise.

Optimizing analysis conditions for high-reliability FCM: balance between flow rate, abort rate, and particles concentrations

Quantification of EVs remains a challenging task and to address this, we have determined the optimal conditions for EVs-FCM experiments. High concentrations of EVs can result in a high number of missed events (high abort rate) and may lead to coincidence of two or more events, detected by the flow cytometer as a single event (swarm effect). To overcome this effect, it is very important to dilute the sample and/or reduce the sample flow rate, ensuring that only individual EVs exceed the threshold and contribute to the signals of the measured events.

In this context, the abort rate is a critical parameter to monitor in EVs–FCM experiments to obtain reliable results.

The ratio between flow speed and sample dilution must be carefully controlled. By modulating/lowering both flow rate and sample concentration, it is possible to find the best conditions to ensure linearity and high reliability on the number of acquired EVs.

Therefore, C16-EVs were serially diluted in 200 nm filtered PBS. We acquired C16-EVs at three different flow rates (slow 10 µl/min, medium 30 µl/min, fast 60 µl/min) and we applied the threshold on fluorescence to better detect and estimate the number of particles. The number of events per second, flow rate, and the percentage of abort rate were recorded in each dilution and summarized in Fig. 3. The results in Fig. 3A demonstrate a decrease in linearity when the abort rate exceeds 5% (dotted red line) and the events per second reach over 5000.

High-speed acquisition (black lines) corresponds to a greater deviation from linearity (r^2= 0.9175) where the maximum acquisition rate is around 18 000 events per second, while in medium- and slow-speed acquisitions the values of r^2 are 0.9780 and 0.9994, respectively. However, the graph in Fig. 3B shows that it is possible to approach a value of r^2 close to one (r^2 = 0.9978) even under conditions of high flow rate (black line), keeping the number of events per second below 5000 and the abort rate below 5%, regardless of the acquisition speed. The concomitant presence of high events per second, high speed, and high abort rate represents the least efficient condition in terms of reliability.

Flow cytometer set up and comparison between V-SSC and fluorescence applied thresholds

As demonstrated previously (Fig. 1), the separation of beads of small size (between 100 nm and 200 nm) is much more efficient on V-SSC compared with B-SSC. Megamix-Plus FSC/SSC beads, a mix of beads that includes those below 200 nm, were used to draw a region including events below 200 nm (Fig. 4A and B black box). The threshold applied on V-SSC allows the visualization of the background noise (Fig. 4B) and the boundary between background signal and fluorescent EVs, necessary to draw the region, is shown in the dot plots of acquired of PBS (Fig. 4C and D). C16-EVs were then analysed applying thresholds on the fluorescent channel or V-SSC channel, showing similar number of events in both conditions (Fig. 4E and F, red numbers in brackets).

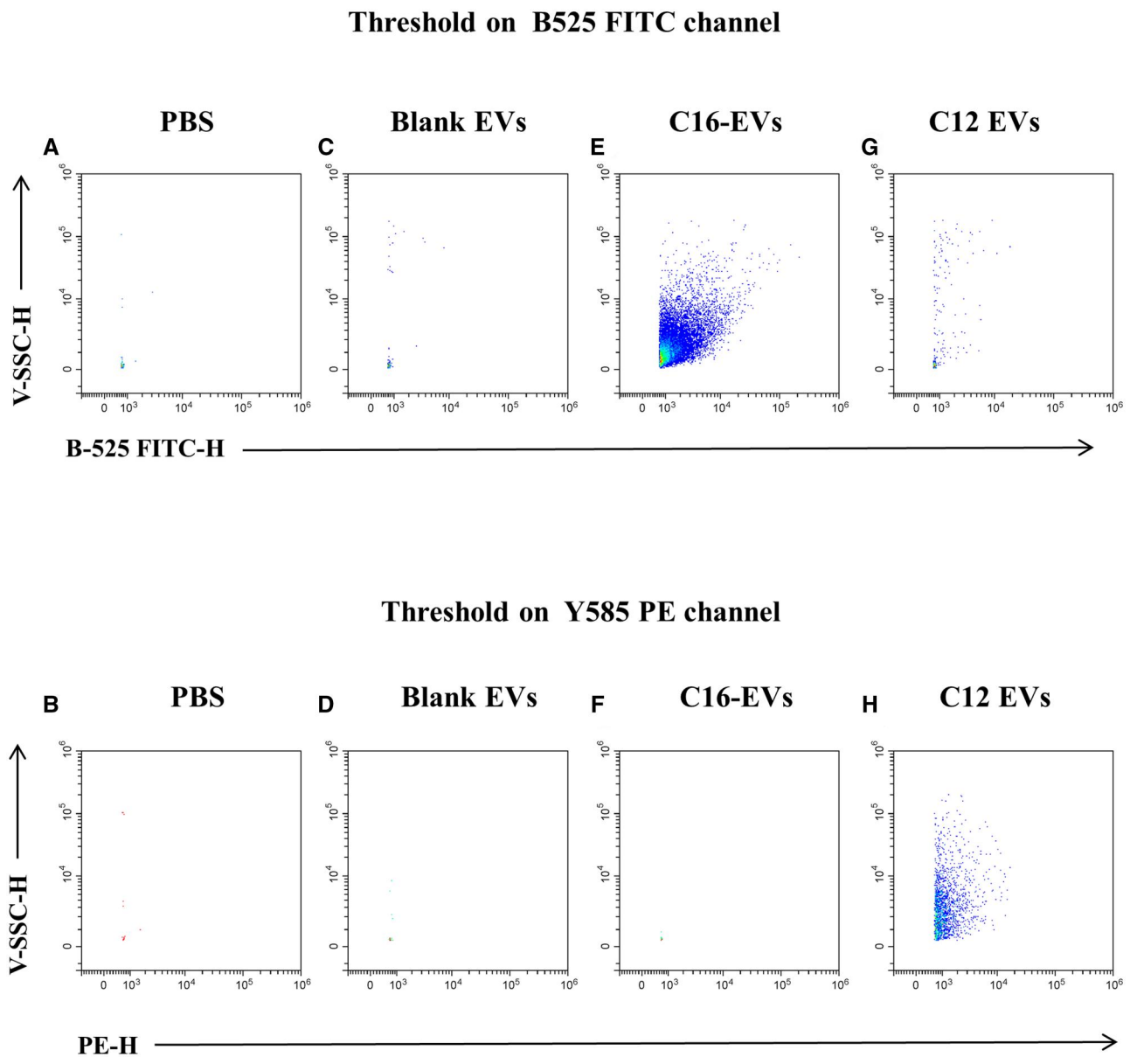

Figure 2. FCM profile of EVs purified from surnatant of A375 melanoma cell line. The dot plots represent FCM analysis of 0.22 μm filtered PBS (**A, B**), blank EVs, (**C, D**), C16-labelled EVs (**E, F**) and C12-labelled EVs (**G, H**). Fluorescent EVs were obtained pulsing cells with BODIPY™ FL C16 or BODIPY™ FL C12. (A, C, E, G) The threshold was applied on green fluorescent channel (B525 FITC channel). (B, D, F, H) The threshold was applied on orange fluorescent channel (Y585 PE channel). The threshold is set to reduce the background signal as much as possible (A, B, C, D) without losing the resolution of the appropriate fluorescent EVs (E, H). The dot plots demonstrate the robustness of the analysis protocol: no events were found when C12-labelled EVs were analysed through green fluorescence threshold (G) as well as no C16-labelled EVs were found through PE fluorescence threshold (F). Results shown are representative of 10 independent experiments

Virus like particles acquisition

As shown previously, we performed a comparison between the two threshold strategies to establish overlapping results in terms of linearity and high reliability in the number of acquired EVs. A greater fluorescent intensity can allow better separation between background noise and fluorescent particles. VLPs used for these experiments were designed to carry the fluorescent fusion protein Gag-GFP. However, these VLPs lack the virulent components of their parent virus, eliminating the possibility that these virus particles could cause an active infection in an exposed individual. Their fluorescence intensity levels are suitable for better separation of VLPs from background signals, allowing a reliable comparison of event counts by using the two different thresholds (Fig. 5A–D). The fluorescent VLPs were acquired at same flow rate and the results are consistent with the previous observations (Figs 3 and 4). The number of VLPs are similar with both applied thresholds, although a full overlap is obtained with a flow rate ≤5000 events per second (Fig. 5E). A slight difference in the number of VLPs was observed above those values when setting the threshold on the fluorescent channel, although not significant (Fig. 5E).

EVs sorting

The most challenging goal is to demonstrate the feasibility of sorting EVs with high efficiency and purity, despite their small size. Since EVs show weak scattering properties and low antigen

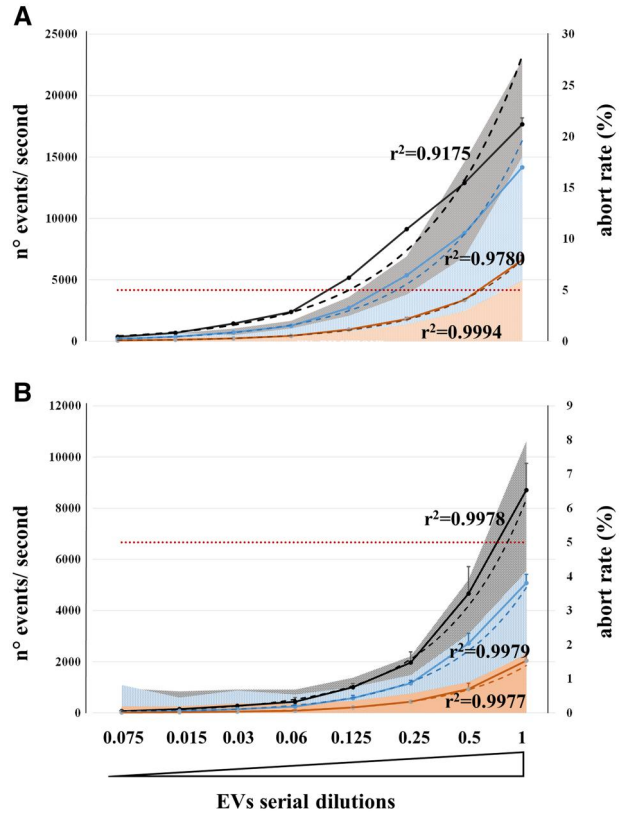

Figure 3. Effect of flow rate, abort rate, and sample concentration on analysis accuracy. Several halving dilutions of C16-EVs was analysed at three different flow rates (red line-slow: 10 µl/min, blue line-medium: 30 µl/min, black line-fast: 60 µl/min) and the number of events per second and the percentage of abort rate were evaluated. The dots on the continuous lines represent the number of events per second (y-axes on the left) at the indicated dilution (x-axes); dashed lines represent the fitted data with exponential model; shaded area represents the abort rate expressed as a percentage (y-axes on the right). (**A**) High speed of acquisition (black line) combined with higher EVs concentration corresponds to a greater deviation from linearity ($r^2 = 0.9175$). Decreasing the flow rate increases the fitting of the model ($r^2 = 0.9780$) until slow flow rate ($r^2 = 0.9994$). Decrease in linearity is observed in all the flow rate conditions when the abort rate is exceeded by 5% (dotted line). (**B**) The graph shows that it is possible to approach a value of r^2 close to 1 even in conditions of high flow rate (black line), keeping the number of events/second below 5000 and the abort rate below 5% (dotted black line). Results are representative of three independent experiments performed in duplicate

densities, having a reliable fluorescent tracer that allows clear identification of the vesicles to be separated from the background noise becomes an essential requirement. Recently, a method referred as 'nanoFACS', has been developed for the detection, analysis, and sorting of EVs and small viruses by FCM [32]. This method has been optimized for use with a customized MoFlo Astrios-EQ Cell Sorter (Beckman Coulter). We performed a similar experiment by using a MoFlo Astrios-EQ equipped with four lasers (405, 488, 561, and 640 nm), 70 µm nozzle, and with applied pressure of 60 psi. Although Morales-Kastresana et al have suggested a different approach [32], we have applied the threshold on 488-SSC (B-SSC) to allow a broader application of the procedure with commonly available instrumental configurations. As a basic strategy, we set a threshold value on B-SSC channel to visualize green fluorescent polystyrene beads of 100 nm, as shown in Fig. 6. Furthermore, to achieve optimal forward scatter (FCS) separation, we tested several masks on dual FSC detectors, identifying the M1 and P1 masks as the best combination. Moreover, we minimize vesicle aggregates and electronic background noise by a gating defined by plotting B-SCC Area channel versus B-SCC Width channel (Figs 6 and 7, and Supplementary Fig. S1). At nanoscale level we do not cut down the noise and the crucial step is to define the right balance between background noise and signal intensity. The strategy employed in the sorter procedure is based on a gradual reduction of the threshold up to the limit of 300 events/second for PBS and 4000 events/second for samples. Additionally, the proportion of events falling within the identified singlet region is balanced with those within the background region. To achieve this balance, the threshold is adjusted so that noise does not exceed 50% of signals detected. This is with a view to reducing the swarm effect, which is applied in the analysis strategy and is fundamental to the sorting process. In detail, as shown in Fig. 6A, a region was drawn to exclude events with a higher B-SSC Width signal: events with low SSC-width. Signals are identified as singlets while doublets and background are distributed in the region with higher SSC-width (Supplementary Fig. S1).

The fluorescent beads Megamix-Plus FSC and SSC are shown in the dot plots (Fig. 6B and D) and histograms (Fig. 6C and E), respectively. Once defined the threshold value on the B-SSC channel and the corresponding voltage to reduce the PBS background noise to less than 300 events/s, we confidently applied a simplified sorting procedure to sort EVs stained with different fluorescent tracers, as shown in Fig. 7. The beads are acquired prior to each sorting experiment and serve to delineate the region within which the particles to sort will be selected. Following the selection of the singlets and the exclusion of background noise (Fig. 7A, SSC-A vs SSC-width), the region corresponding to the Megamix below 300 nm is selected (Fig. 7B). The population to be sorted is then selected based on the relative fluorescence (Fig. 7C); the last step is the post-sorting analysis which allows to evaluate the purity and efficiency of the sorting (Fig. 7D).

Figure 8 shows the sorting experiment of a sample consisting of C12- and C16-EVs, produced separately from two different cell cultures and subsequently mixed. As shown in Fig. 8B, EVs released by unstained cells were used as negative control (blank EVs). Figure 8C illustrates the cytofluorimetric profile of mixed C12-C16 EVs: quadrants Q1 and Q3 represent the region where C12-EVs and C16-EVs fall, respectively. As this is an analysis in which the sample is not double labelled, the events falling in quadrant Q2 are attributable to both a coincidence and a swarm effect of the EVs [27, 28]. Furthermore, it is important to underline that, despite the refinement of the sorting protocol, it is not possible to eliminate the electronic background noise (quadrant Q4) [33]. Therefore, the respective purities of sorted EVs must be evaluated considering exclusively the positive quadrants for the fluorescent signals (Q1, Q2, and Q3). The small gate inside each post-sorting control plot indicates the level of purity reached after sorting (in red, $Q1_r$, $Q2_r$, and $Q3_r$). Reanalysis of the C12-EVs and C16-EVs populations show high levels of purity (98.0% $Q1_r$ in Fig. 8D, and 96.6% $Q3_r$ in Fig. 8E), while a non-significant number of EVs was identified outside specific gate (Q2+Q3 or Q2+Q1, respectively) evidencing the consistency of the method. Moreover, Fig. 9 clearly illustrates the reliability of the method we have developed. Figure 9 shows double-labelled samples of EVs, Ceramide/C16 EVs (Fig. 9A), and C12/Nef^{mut}-GFP EVs (Fig. 9D), from which different sub-populations were derived. In detail, fluorescent EVs were obtained from cells pulsed with both C16 and Ceramide, a red-fluorescent dye (λex 589 nm/λem 616 nm).

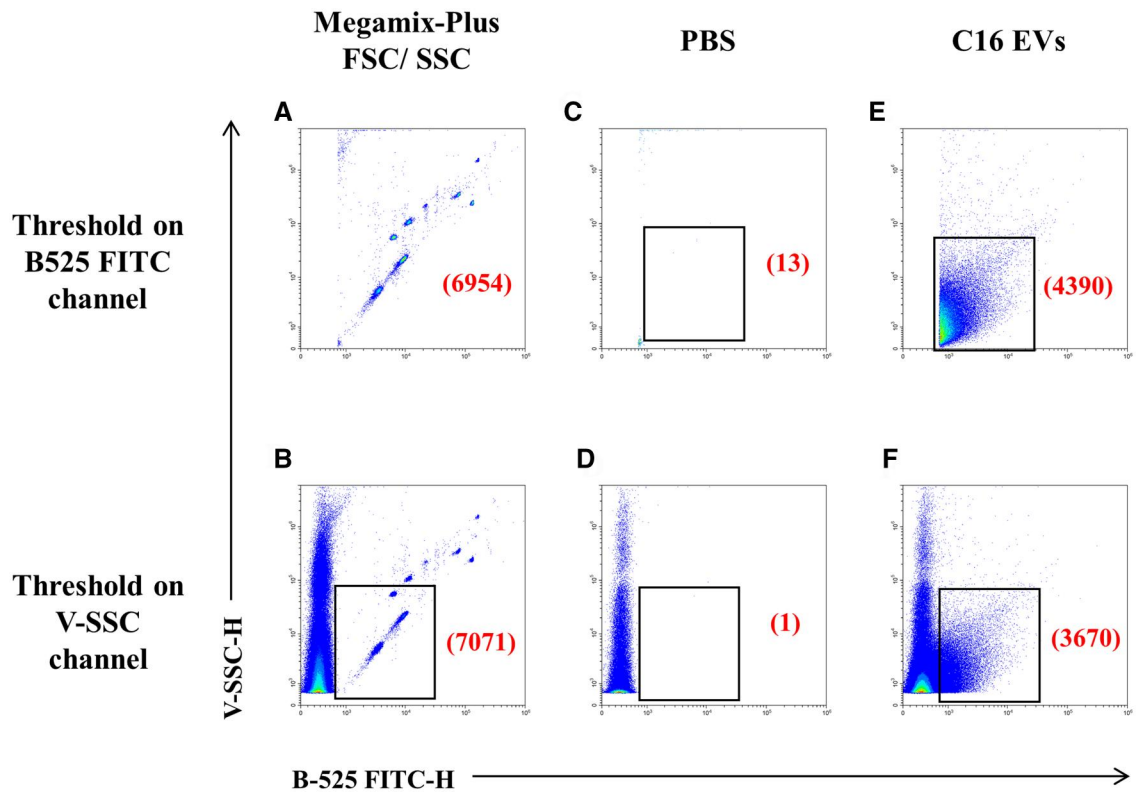

Figure 4. Comparison between V-SSC and fluorescence applied thresholds. Representative density plots of reference beads (Megamix Plus FSC/SSC), analysed applying the threshold on the fluorescence or on the V-SSC channels, are shown in (**A**) and (**B**), respectively. PBS filtered at 0.22 μm was used to exclude the background noise (**C, D**). The black boxes were drawn to include the smallest sized beads (<200 nm) and to exclude the background noise. The C16 EVs that fall in the black box were enumerated (**E, F**). The numbers in red, inside the dot plots (C), (D), (E), and (F), indicate the events per μl

Even though the two tracers, Ceramide and C16, were differently distributed on the EVs (Q1 = 3.54% vs Q3 = 37.5%, respectively, Fig. 9A), the result of re-analysis shows a remarkable quality of the sorting (96.2% and 95.3%, respectively, Fig. 9B and C). Similar experiments were performed using cells transfected with a construct that carries a Nef^{mut}-GFP fusion gene and incubated with C12 to obtain different EVs populations. The results, once again, demonstrate the feasibility of the protocol to sort EVs, allowing for C12-EVs and GFP-EVs purities of 94.6% and 97.3%, respectively (Fig. 9E and F). The post-sorting purity of GFP Nef^{mut}-positive EVs population is ~86%, slightly lower than the others (Fig. 9G). In conclusion, the high purity achieved after sorting, on specific EVs populations, demonstrates the reliability of the developed protocol and the high quality of the procedure, regardless of the fluorescence channel and the characteristics of the fluorochrome. To provide further support for the sorting strategy and to have direct evidence of EVs size, NTA analysis was conducted on EVs sorted from a double-labelled C12-C16 EVs population. As illustrated in Fig. 10, double labelled C12-C16 EVs were sorted into the three populations: $C12^+C16-$ EVs (Q1), $C12-C16^+$ EVs (Q3) and $C12^+C16^+$ EVs (Q2) (Fig. 10A). The dot plot B, C, and D show FCM post-sorting re-analysis of the sorted populations and reveal a reached purity of 92.9% for $C12^+C16-$ EVs, 99.0% for C12–C16+ EVs and 98.4% for C12+C16+ EVs, respectively. Furthermore, NTA gives accurate predictions of the sizes and demonstrates that the size distribution of sorted population is as follows (expressed as mode): 86.3 +/− 5.5 nm for $C12^+$ C16− EVs, 75.9 +/−6.3 nm $C12-C16^+$ EVs and 62.3 +/− 34.9 nm $C12^+$ $C16^+$ EVs (Fig. 10F–H, respectively). NTA analysis has been performed also on pre-sorting EVs and reveals a distribution in size of 155.1 +/− 7.2 nm (Fig. 10E). The negative population (Q4) was also selected in the experiment (data not shown), which includes unmarked EVs (as well as background noise, doublets, electronic signals, and salts in the sheath fluid). The NTA analysis of Q4 reveals a size distribution as a mode of 153.7 ± 18.4 nm.

Discussion

EVs are a heterogeneous population of micro- or nano-membrane-bound particles involved in different biological functions. They play a role in communication between cells and organs, by carrying many classes of molecules that act as biochemical or molecular signals. They are characterized by a great heterogeneity in pathway generation, composition of bilayer, their cargo [4, 5]. EVs can transport a variety of proteins, including growth factors, receptors, and cytokines, as well as lipids, nucleic acids, and metabolites, depending on their biogenesis. Furthermore, there is also a wide diversity in their size distribution: size range of EVs starts at ~30 nm up to over 300 nm with a peak at a diameter of 100 nm [5, 34]. EVs have garnered a lot of attention for their potential applications in diagnosis and their therapeutic potential [35]. As well as EVs, VLPs are small particles of 20–200 nm that can be exploited as carriers for small molecules and are an attractive and versatile tool for the design of vaccines and therapeutics. Given the varying identities of these particles, a standardized approach is required to ensure reliable and accurate results for reproducible measurements and downstream applications. Minimal requests for reliable analysis technique are

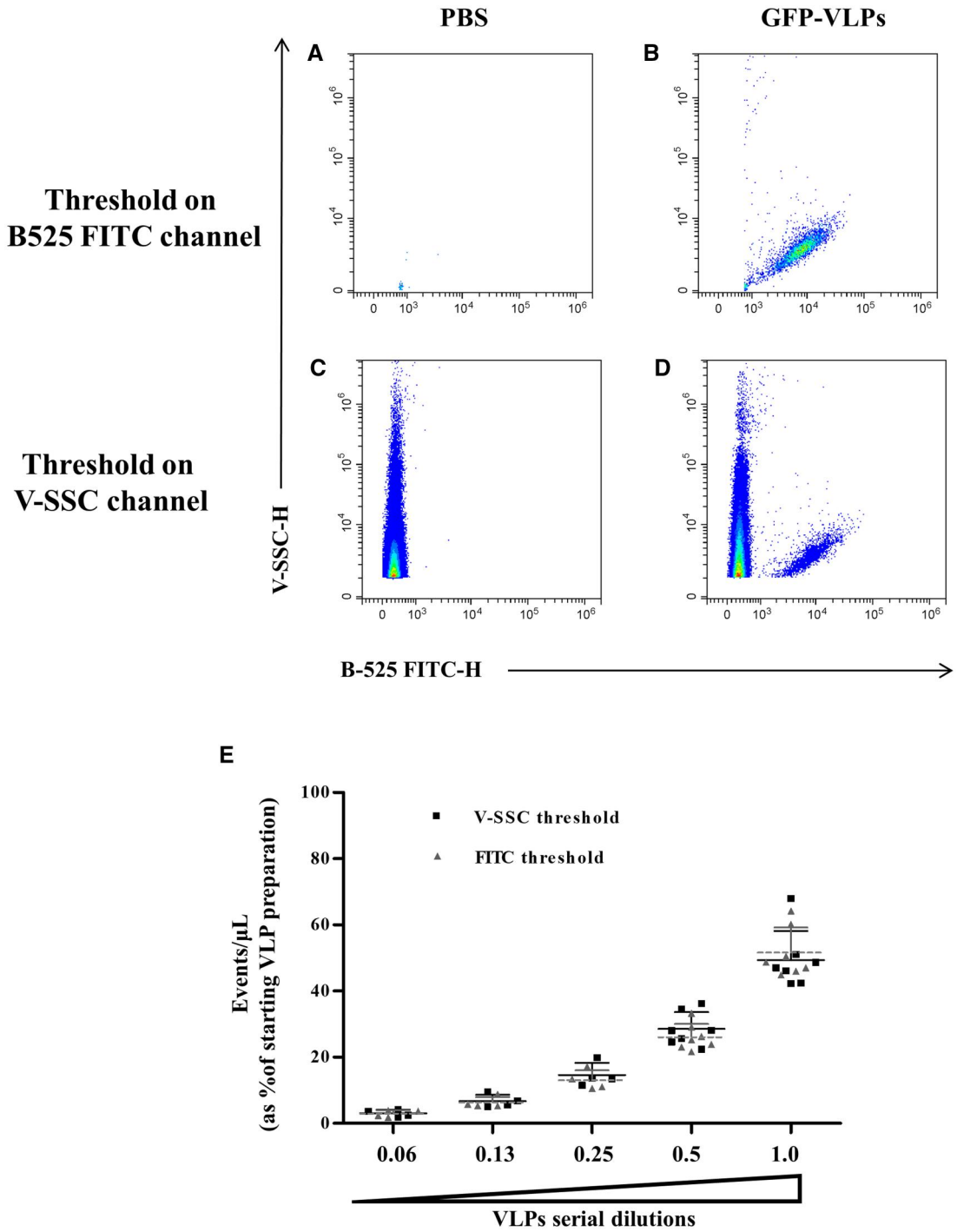

Figure 5. High reliability on the number of acquired nanoparticles. VLPs that carry fluorescent fusion protein Gag-GFP (GFP-VLPs) were quantified through the two different threshold strategies: (**A, B**) threshold on green fluorescent channel; (**C, D**) threshold on V-SSC channel. PBS buffer 0.22 µm filtered (A, C) was used to determine instrument background noise. The black boxes were drawn to include fluorescent VLPs (<200 nm) and to exclude the background noise. (**E**) The graph summarizes serial dilution of VLPs count using the two different threshold strategies. The two series of data have a good fit ($r^2 > 0.995$) as demonstration of the robustness of the method through counting with the two different threshold strategies. Count is expressed as percentage of starting VLPs preparation. Each experimental session was run with same acquisition settings (flow rate of 10 µl/min, threshold and gain value). The grey and black error bars indicate the SD of samples acquired with the threshold applied on fluorescent or V-SSC channels, respectively. No significant difference was observed

standardization of isolation methods; optimization of EVs cargo analysis; accurate size-based quantification [36, 37]. Various techniques try to respond to these methodological needs. For the purification of vesicles below 200 nm in size, size exclusion chromatography and asymmetric flow field-flow fractionation are commonly used isolation techniques. Quantification methods such as microscopy (scanning/transmission EM and atomic force microscopy), DLS, NTA, FCM, and small-angle X-ray scattering can be cited [10, 11, 38]. FCM is a technique that offers several advantages, and as such, it has received significant attention. In detail, FCM is a low-time-consuming and high-throughput technique allowing high reproducibility, and in many cases, it may

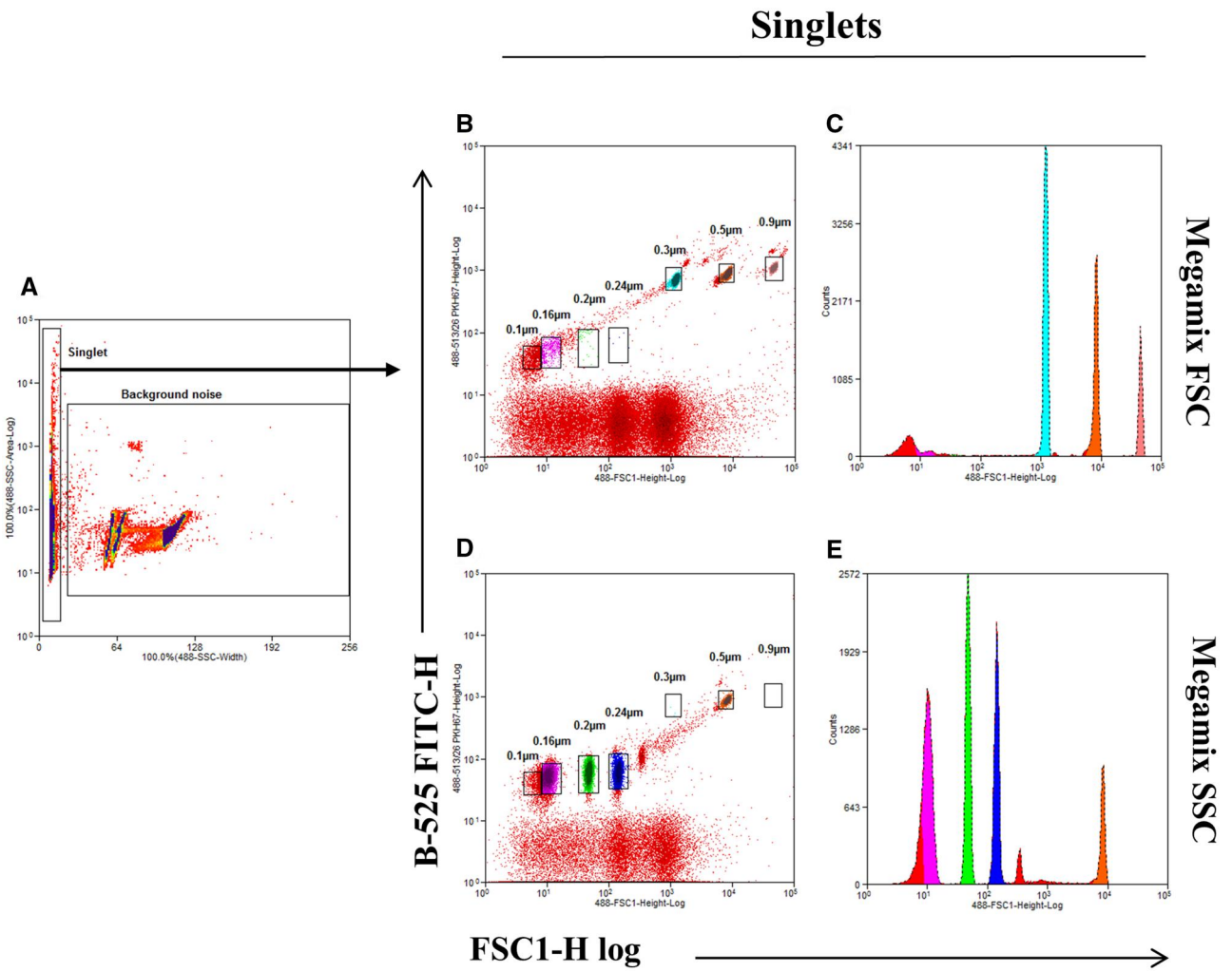

Figure 6. Threshold setting to define gating strategy for EVs sorting. The B-SCC Area signal versus B-SCC Width signal allowed the exclusion of vesicle aggregates and background noise from the population of singlet particles (**A**) Representative dot plots and respective histograms of singlet gated Megamix-Plus FSC (**B, C**) and SSC (**D, E**) polystyrene beads with size between 100 and 900 mm (0.1, 0.16, 0.2, 0.24, 0.3, 0.5, and 0.9 µm). The analysis was performed on the events falling in the singlet region (see black arrow)

require low sample manipulation. The primary challenge is the detection limit, as it has mainly been used in cellular analyses or functional assays. Conventional FCM is not sensitive enough to detect EVs by morphological parameters. At nano-scale dimensions, there is not a linear relationship between light scatter and dimension, making the detection of EVs a challenge [39, 40]. However, technological advances in new FCM have led to a significant improvement in the dimensional resolution, although there are still no tools capable of clearly identifying and quantifying EVs based solely on physical or morphological parameters. This study will optimize an FCM procedure for detecting nanoparticles with confidence. A straightforward protocol has been proposed for the reliable detection, quantification, and sorting of EVs released by cells in culture supernatants. The experience gained from the use of the Gallios cytofluorimeter [30], has been successfully applied to the Cytoflex LX cytofluorimeter that boasts a wide linear dynamic range, resulting in improved resolution of dim and bright populations. In conventional FCM protocols, a linear scale is used for light scatter measurements whereas a log scale is used for fluorescence signals, excluding some analyses such as the cell cycle. In contrast, submicron particles are analysed by non-conventional FCM settings, and scatter signals (FSC or SSC) are visualized with log scales. Furthermore, the threshold is set to remove signals primarily derived from debris and electronic background. Moreover, FCM instruments exhibit high background noise when calibrated for the analysis of small particles (approximately <200 nm). Using SSC downstream of other lasers, such as the violet laser (405 nm) or yellow laser (561 nm), will significantly improve instrument sensitivity, as suggested by Morales-Kastresana et al. [32]. However, the chances of success increase when employing fluorescence signals, which are essential for identifying particles below 200 nm, separating them from background noise and debris [30, 33]. Our study confidently presents results on the detection, quantification, and sorting of EVs. Identifying EVs smaller than 200 nm has been the first challenge. However, with the use of a fluorescent tracer, EVs can be accurately visualized even though conventional flow cytometers lack the capability to identify smaller particles based solely on their physical characteristics (Forward and Side Scatter). The second drawback was the selection of the parameter on which to apply the threshold. Our experience and the latest publications have highlighted the importance of fluorescence in visualizing nano-sized particles. Nevertheless, it is also feasible to utilize the enhanced sensitivity of SSCs when excited by lasers other than blue, thus eliminating the need for fluorescence. In our experimental setting, we used C16-EVs, a population of metabolically labelled

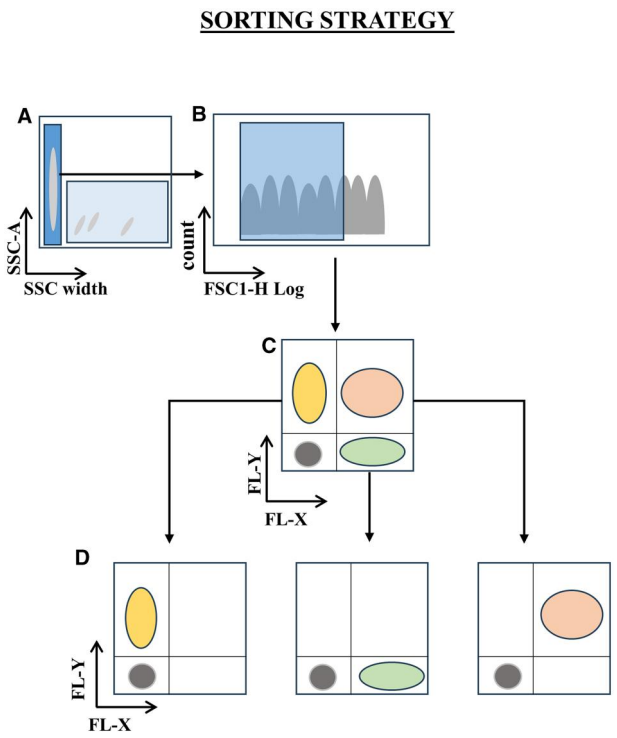

Figure 7. Gate strategy for EVs sorting. The figure shows the gate strategy applied for EVs or VLPs sorting experiments. In detail, following the calibration beads, the sample to be sorted is acquired. The selection of singlets region (**A**, light blue box on low 488-SSC-Width) is followed by gate on region in which the beads fall below 300 nm (**B**, light blue box). The region of the populations to be sorted is then selected based on the specific fluorescence channel (**C**, FL-X and FL-Y). A post-sorting analysis is conducted after each sorting procedure to derive the purity of the sorted population (**D**)

EVs, approximately 80 nm in size [14]. We decided to exclude direct-labelled EVs with fluorescent tracers or with specific fluorochrome-conjugated antibodies because standardized procedures to eliminate or reduce the presence of non-specific events are still under investigation [33, 41]. As shown in Fig. 1, we demonstrated that we successfully detected fluorescent particles around 100 nm by using V-SSC. The RI was employed to assess the impact of the V-SSC on the relative peak resolution of the smaller spheres. The data demonstrate that a higher RI of V-SSC enables the visualization of a broader distribution of EVs, which is not discernible with B-SSC (which focuses specifically on the bead region between 100 and 200 nm). This is corroborated and reinforced by the elevated mean values and a narrower CV obtained with V-SSC in comparison to B-SSC (Table 1).

Additionally, we compared the number of events (C16-EVs) obtained by applying the threshold on the SSC parameter with that applied on the fluorescence channel (Fig. 4).

In summary, our data confirm that applying the threshold on the violet laser (V-SSC) is more efficient in separating beads of different sizes than applying the threshold on the blue laser (B-SSC). Furthermore, we can clearly identify the EVs with a high level of correspondence by applying the threshold on the physical parameters, even without fluorescence. The main pitfall for a correct EVs quantification is the swarm effect and efforts should be made to avoid or greatly reduce multiple detections of EVs. The present study has revealed that a harmonious balance of speed, concentration, and abort rate is essential in obtaining precise measurements of the particles being analysed. The optimal conditions for flow rate and sample concentration were determined to ensure linearity in the quantification of EVs. Furthermore, in addition to the observations previously reported in Lucchetti et al. [15], precise numerical references were provided to ensure the accuracy of the analysis and the maintenance of the linearity range. As demonstrated in Fig. 3, we delineate the event rate (which must remain below 5000 events per second) and the abort rate percentage (which must be maintained below 5%) to ensure analysis linearity, calculated as r^2. In particular, the acquisition speed of individual events per time unit is significant in reducing the percentage of abort rate (Fig. 3). This parameter is crucial for establishing a window in which it is possible to define linearity conditions between flow rate, abort rate, and EVs concentrations. In our working conditions, the limit of abort rate to maintain linearity has been set at 5%. Utilizing this value enhances the acquisition speed while maintaining a linear regime (see Fig. 3B).

Furthermore, to demonstrate the method's robustness, we confidently enumerated C16-EVs using V-SSC or fluorescence thresholds, resulting in an excellent match of recorded events (Fig. 4). The same protocol was successfully applied to analyse GFP-VLPs. Once again, the robustness of the method is highlighted, which exactly enumerates the particles analysed with both the V-SSC and fluorescent thresholds (Fig. 5), despite the impact of background noise. It is recognized that background noise exerts a substantial influence on the number of highlighted events; consequently, while its complete elimination remains infeasible, its impact can be mitigated through the implementation of appropriate dilutions and a balanced threshold. Applying the threshold on the corresponding fluorescent channel for the quantitative evaluation of fluorescent EVs significantly reduces the background noise during acquisition compared to the background noise detected with standard protocols (SSC threshold). The use of a fluorescent threshold has already been demonstrated in the detection of EVs using conventional non-customized flow cytometer. New instruments with increased sensitivity enable better visualization of events below 200 nm. Although standardization of light scattering and fluorescence data between different flow cytometers remains a challenge, new instruments with increased sensitivity allow better visualization of events below 200 nm.

Applying these suggestions has enabled the development of sorting strategies that utilize the threshold on the blue laser (B-SSC) with confidence. Our results demonstrate that EVs sorting can provide reliable and accurate results even when using the B-SSC threshold. The SSC-W versus SSC-A combination helps us define the region in which the EVs fall and discriminate them from the background noise. Background noise is the dominant factor preventing the resolution of nanoscale events, like EVs. The background is determined by doublets, electronic signals, salts in the sheath fluid, and can affect or compromise the resolution.

By separating vesicles labelled with different fluorescent tracers, a high level of purity can be achieved using cell sorters with well-defined parameters. As shown in Figs 8 and 9 we reached a post-sorting purity of over 95%. The size of pre- and post-sorted EVs is shown in Fig. 10. These results demonstrate that the size of the sorted particles is consistent with the findings of the initial stages of the protocol. Furthermore, the sensitivity of the experimental protocol and the specificity of the sorted particles have been validated. It is also noteworthy that the sorted particles exhibit a range of sizes, with a mode distribution of approximately 60–90 nm (Fig. 10F–H).

Furthermore, results highlight that the total EVs population is heterogeneous in size, including white vesicles (which fall within the negative background region) and contribute to the size distribution determined during pre-sorting. The small size of the

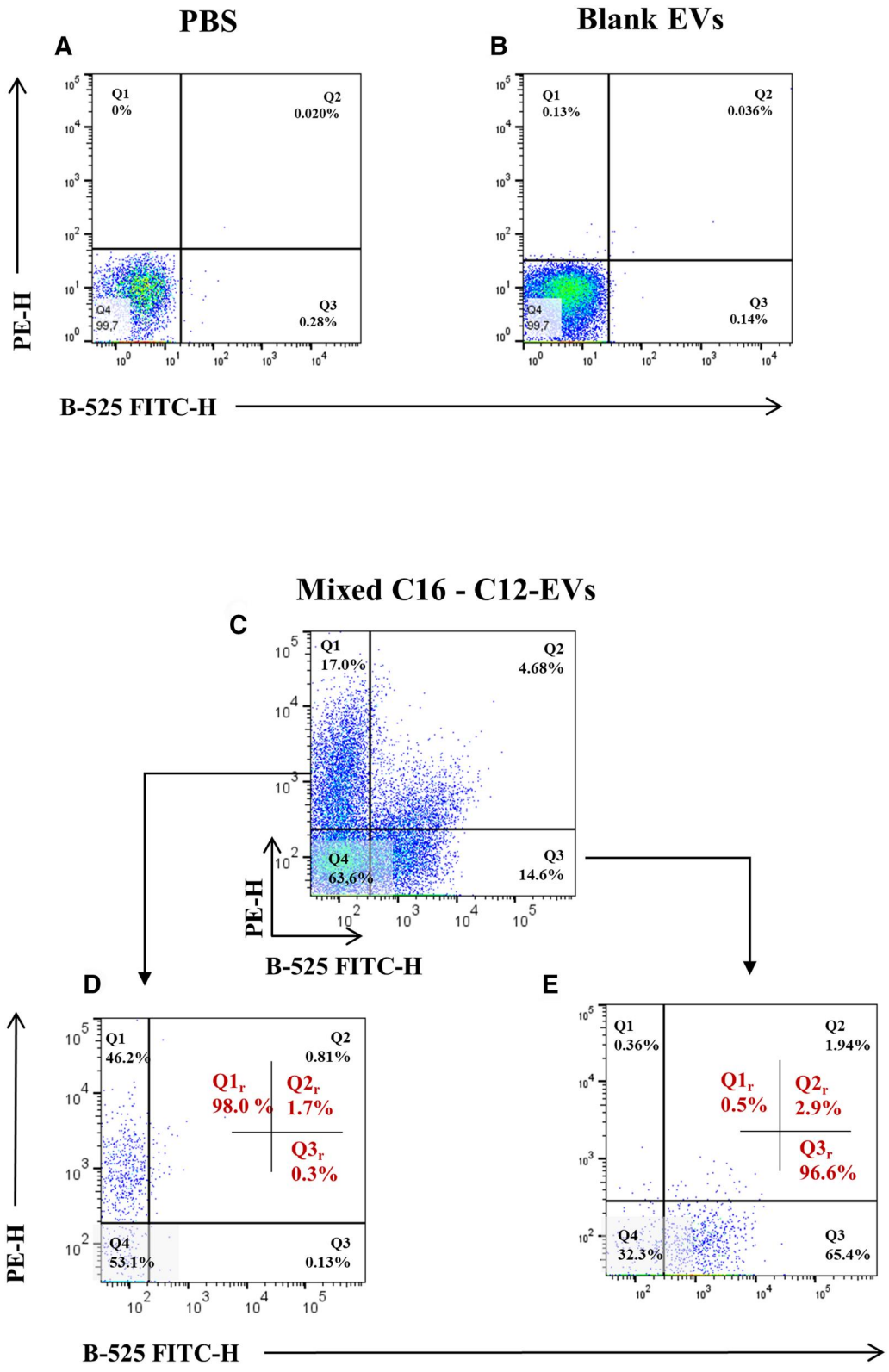

Figure 8. Sorting of fluorescent mixed C16 and C12 EVs. Representative dot plot of background noise assessed by PBS acquisition (**A**) EVs released by unpulsed cells were used as negative control for the fluorescent populations (**B**). Dot Plot of mixed C16- and C12-labelled EVs are shown in (**C**). Re-analysis of sorted C12- and C16-labelled EVs are shown in (**D**) and (**E**), respectively. The small gate (red) inside the plots indicates the values of the positive quadrants for fluorescent signals ($Q1_r$, $Q2_r$, and $Q3_r$). The purity post sorting is expressed as a percentage of the sum of the positive quadrants (Q1 + Q2 + Q3). The limitations of current flow cytometry technology cannot eliminate systemic background noise present in the quadrant Q4 that is excluded from the calculation of the positive EVs. The events falling in quadrant Q2 are attributable to both a coincidence and a swarm effect of acquired EVs. The experiment shown is representative of five independently performed experiments

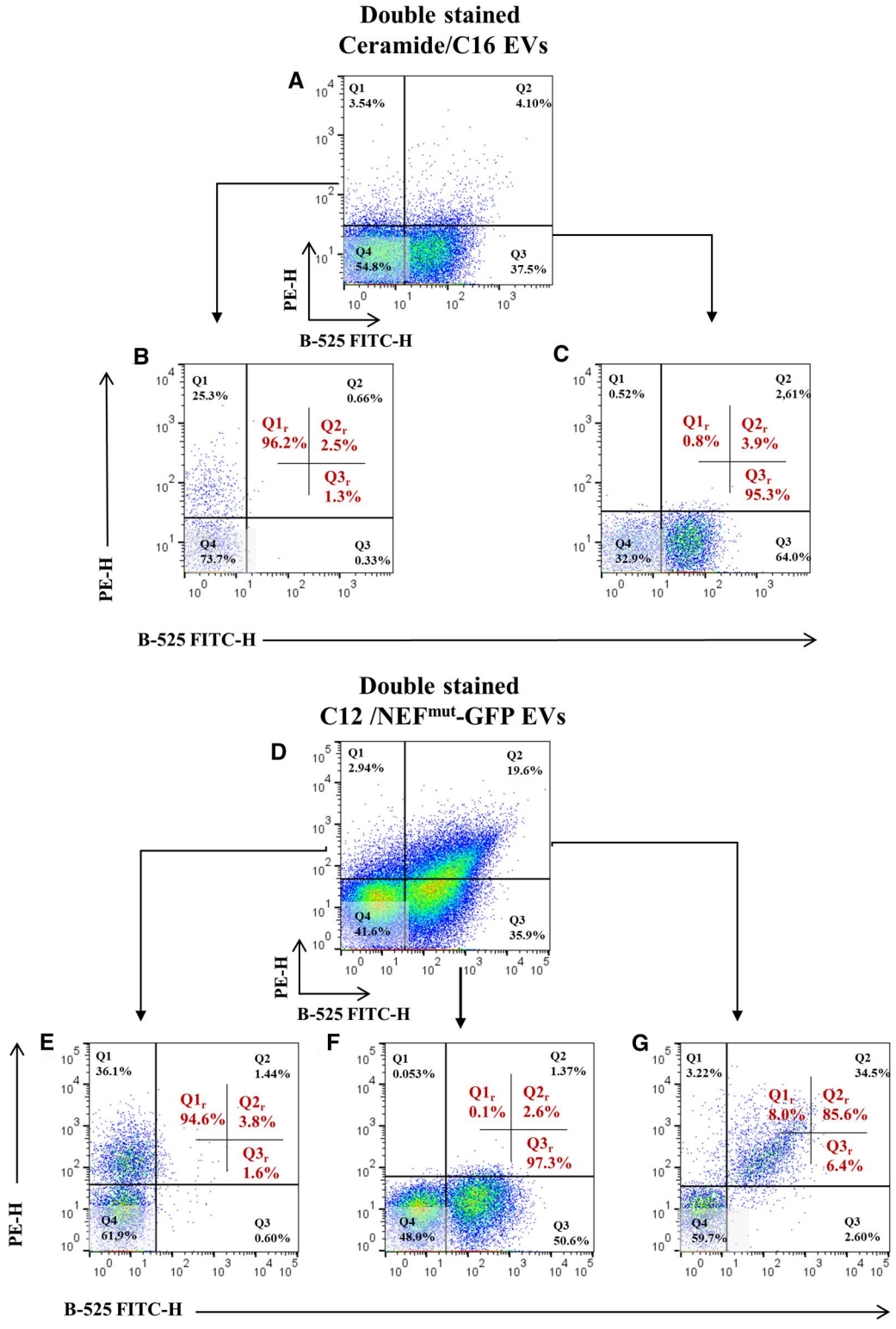

Figure 9. High resolution sorting of Ceramide-C16 EVs and C12-Nef GFP EVs. The reliability of sorting tested on EVs sample obtained from cells incubated with C16 and Ceramide (**A–C**), and EVs sample released by cells transfected with a construct that carries a Nef^{mut}-GFP fusion gene and incubated with C12 (**D–G**). The EVs population before sorting are shown on the dot plots (A) and (D), respectively. Reanalysis of sorted EVs positive for a single fluorescence are shown on dot plots (B), (C), (E), (F), and (G). The small gate (red) inside the dot plot indicates the post sorting purity, expressed as a percentage of the sum of the positive quadrants

sorted fluorescent vesicles confirms the success of the sorting. These data support the results reported in Barreca *et al.* [14], where it was demonstrated by EM analysis that sorted C16-EVs have a size of 80 nm, while characterizing the other vesicles provides the basis for further studies.

The proposed protocol builds upon the methodology developed by Coscia *et al.* [30] and further refined by our research group. It employs fluorescence as a means of visualizing and investigating nanoscopic particles. This approach has been successfully applied to the study of EVs derived from cell cultures

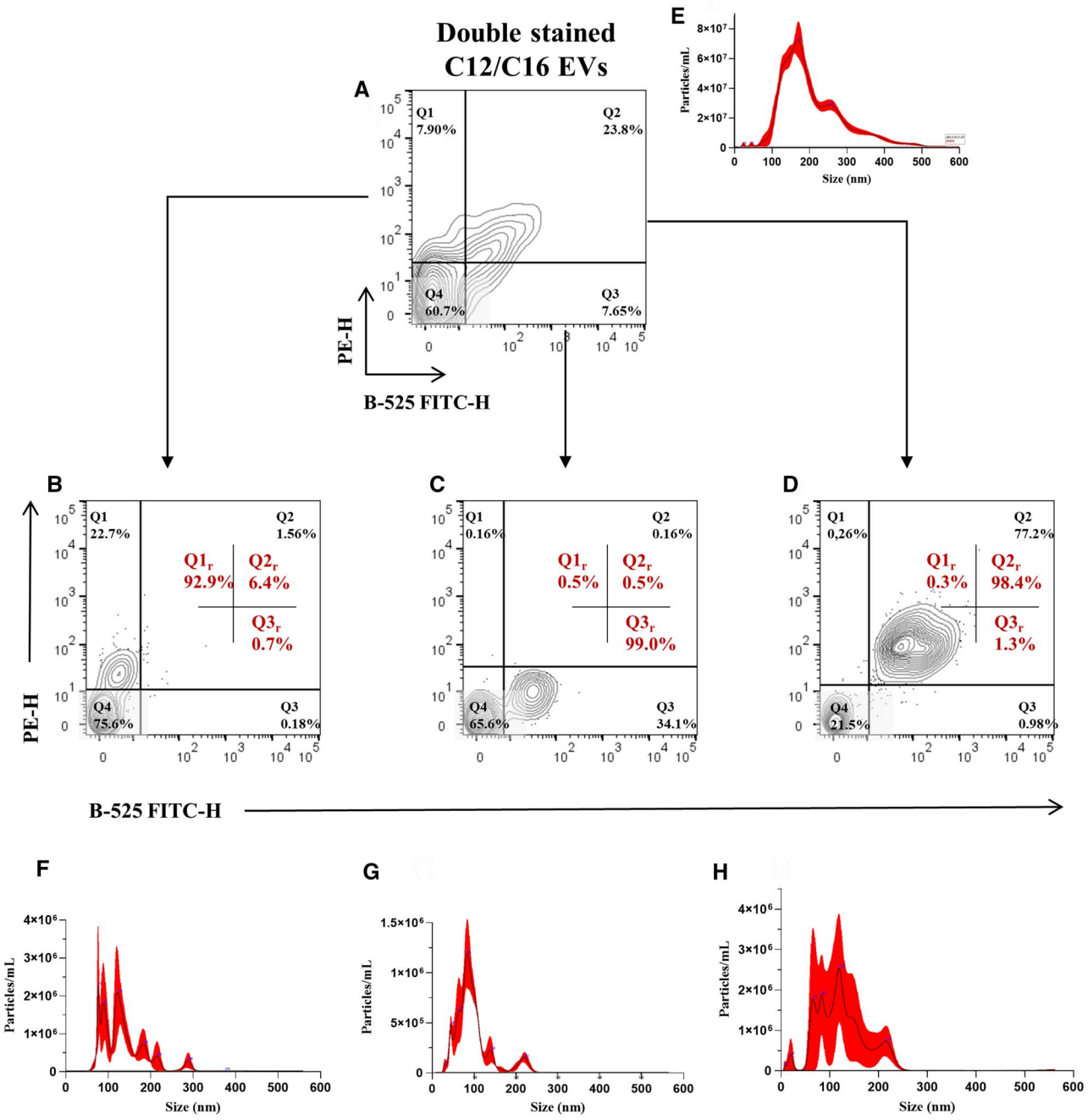

Figure 10. Sizing of C12-C16 EVs population. The dot plots in the figure represent double-labelled C12-C16 EVs (**A**), which were sorted into the three populations. The EVs were classified into three populations: $C12^{+}C16^{-}$ (Q1), $C12^{-}C16^{+}$ (Q3) and $C12^{+}C16^{+}$ (Q2). In Figures (**B–D**), the results of the FCM re-analysis and the purity of the post-sorting populations are presented. The small gate (red) inside the dot plot indicates the post sorting purity, expressed as a percentage of the sum of the positive quadrants. Figure (**E–H**) represent the respective NTA analyses and show the size distribution (nm) of the total (155.1 ± 7.2 nm) and sorted populations ($C12^{+}$ 86.3 ± 5.5 nm; $C16^{+}$ 75.9 ± 6.3 nm; $C12^{+}/C16^{+}$ 62.3 ± 34.9 nm). The results are expressed as mode ± SD. Results are representative of two independent experiments

subjected to pulse and chase with fluorescent probes. We present this as a streamlined approach for studying EVs in controlled settings, such as *in vitro* systems. However, it should be noted that the development of a robust staining, detection, and sorting protocol for fluorescent EVs is a challenging endeavour. Several efforts were made in choosing the probes to use for labelling EVs, depending on the experimental needs we had. It is evident that this approach is well suited to controlled systems; however, it must be adapted for the study of biological samples.

Acknowledgements

The authors acknowledge Dr Francesco Manfredi (Istituto Superiore di Sanità, Rome) for providing the plasmid encoding Nef^{mut}-GFP.

Supplementary data

Supplementary data is available at *Biology Methods and Protocols* online.

Author contributions

Valentina Tirelli (Conceptualization [equal], Data curation [equal], Formal analysis [equal], Investigation [equal], Methodology [equal], Software [equal], Validation [equal], Visualization [equal], Writing—original draft [equal], Writing—review & editing [equal]), Felicia Grasso (Conceptualization [equal], Data curation [equal], Formal analysis [equal], Investigation [equal], Methodology [equal], Software [equal], Validation [equal], Visualization [equal], Writing—review & editing [equal]), Valeria Barreca (Data curation [supporting], Formal analysis [supporting], Methodology [supporting], Writing—review & editing [supporting]), Deborah Polignano (Methodology [supporting]), Alessandra Gallinaro (Investigation [Supporting], Methodology [Supporting]), Andrea Cara(Funding acquisition [supporting], Methodology [supporting], Resources [supporting]), Massimo Sargiacomo (Funding acquisition [equal], Investigation [supporting], Methodology [supporting], Resources [equal]), and Maria Luisa Fiani (Data curation [supporting], Investigation [supporting], Methodology [supporting], Writing—original draft [supporting], Writing—review & editing [supporting]), Massimo Sanchez (Conceptualization [lead], Data curation [equal], Formal analysis [equal], Investigation [equal], Methodology [lead], Project administration [lead], Software [equal], Supervision [lead], Validation [equal], Visualization [equal], Writing—original draft [lead], Writing—review & editing [equal])

Conflict of interest statement. The authors declare that they have noconflict of interest.

Funding

The study received support from internal funds provided by the Istituto Superiore di Sanità; by a grant from Italian Ministry of Health, Ricerca Finalizzata RF-2019-12369719 and by EU funding within the Next Generation 8 Extended Partnership initiative on Emerging Infectious Diseases (Project no. PE00000007, INF-ACT).

References

1. Jeppesen DK, Zhang Q, Franklin JL, Coffey RJ. Extracellular vesicles and nanoparticles: emerging complexities. *Trends Cell Biol* 2023;**33**:667–81. https://doi.org/10.1016/j.tcb.2023.01.002
2. van Niel G, D'Angelo G, Raposo G. Shedding light on the cell biology of extracellular vesicles. *Nat Rev Mol Cell Biol* 2018;**19**:213–28. https://doi.org/10.1038/nrm.2017.125
3. van Niel G, Carter DRF, Clayton A *et al.* Challenges and directions in studying cell–cell communication by extracellular vesicles. *Nat Rev Mol Cell Biol* 2022;**23**:369–82. https://doi.org/10.1038/s41580-022-00460-3
4. Zhou X, Jia Y, Mao C, Liu S. Small extracellular vesicles: non-negligible vesicles in tumor progression, diagnosis, and therapy. *Cancer Letters*, 2024;**580**:216481. https://doi.org/10.1016/j.canlet.2023.216481
5. Bordanaba-Florit G, Royo F, Kruglik SG, Falcón-Pérez JM. Using single-vesicle technologies to unravel the heterogeneity of extracellular vesicles. *Nat Protoc* 2021;**16**:3163–85. https://doi.org/10.1038/s41596-021-00551-z
6. Kilinc S, Paisner R, Camarda R *et al.* Oncogene-regulated release of extracellular vesicles. *Dev Cell* 2021;**56**:1989–2006.e6. https://doi.org/10.1016/j.devcel.2021.05.014
7. Duan L, Li X, Ji R *et al.* Nanoparticle-based drug delivery systems: an inspiring therapeutic strategy for neurodegenerative diseases. *Polymers (Basel)* 2023;**15**:2196. https://doi.org/10.3390/polym15092196
8. Nooraei S, Bahrulolum H, Hoseini ZS *et al.* Virus-like particles: preparation, immunogenicity and their roles as nanovaccines and drug nanocarriers. *J Nanobiotechnol* 2021;**19**:59. https://doi.org/10.1186/s12951-021-00806-7
9. Akbar A, Malekian F, Baghban N *et al.* Methodologies to Isolate and purify clinical grade extracellular vesicles for medical applications. *Cells* 2022;**11**:186. https://doi.org/10.3390/cells11020186
10. Diehl JN, Ray A, Collins LB *et al.* A standardized method for plasma extracellular vesicle isolation and size distribution analysis. *PloS One* 2023;**18**:e0284875. https://doi.org/10.1371/journal.pone.0284875
11. Dumčius P, Mikhaylov R, Zhang X *et al.* Dual-wave acoustofluidic centrifuge for ultrafast concentration of nanoparticles and extracellular vesicles. *Small* 2023;**19**:e2300390. https://doi.org/10.1002/smll.202300390
12. Gul B, Syed F, Khan S *et al.* Characterization of extracellular vesicles by flow cytometry: challenges and promises. *Micron* 2022;**161**:103341. https://doi.org/10.1016/j.micron.2022.103341
13. Hendrix A, Lippens L, Pinheiro C *et al.* Extracellular vesicle analysis. *Nat Rev Methods Primers* 2023;**3**:1–23. https://doi.org/10.1038/s43586-023-00240-z
14. Barreca V, Boussadia Z, Polignano D *et al.* Metabolic labelling of a subpopulation of small extracellular vesicles using a fluorescent palmitic acid analogue. *J Extracell Vesicles* 2023;**12**:e12392. https://doi.org/10.1002/jev2.12392
15. Lucchetti D, Battaglia A, Ricciardi-Tenore C *et al.* Measuring extracellular vesicles by conventional flow cytometry: dream or reality? *Int J Mol Sci* 2020;**21**:1–15. https://doi.org/10.3390/ijms21176257
16. De Alteriis E, Incerti G, Cartenì F *et al.* Extracellular DNA secreted in yeast cultures is metabolism-specific and inhibits cell proliferation. *Microb Cell* 2023;**10**:277–95. https://doi.org/10.15698/mic2023.12.810
17. Palomba E, Tirelli V, de Alteriis E *et al.* A cytofluorimetric analysis of a Saccharomyces cerevisiae population cultured in a fed-batch bioreactor. *PLoS ONE* 2021;**16**:e0248382. https://doi.org/10.1371/journal.pone.0248382
18. Wei Y, Zhao Z, Wan S *et al.* Flow cytometry-based cell cycle synchronization and transcriptome analysis in cotton (Gossypium arboretum L.). *Ind Crop Prod* 2023;**201**:116889. https://doi.org/10.1016/j.indcrop.2023.116889
19. Xu Q, Liu S, Ji S *et al.* Development and application of a flow cytometry-based method for rapid and multiplexed quantification of three foodborne pathogens in chicken breast. *LWT* 2022;**163**:113487. https://doi.org/10.1016/j.lwt.2022.113487
20. Arkesteijn GJA, Lozano-Andrés E, Libregts SFWM, Wauben MHM. Improved flow cytometric light scatter detection of submicron-sized particles by reduction of optical background signals. *Cytometry Pt A* 2020;**97**:610–9. https://doi.org/10.1002/cyto.a.24036
21. van der Pol E, de Rond L, Coumans FAW *et al.* Absolute sizing and label-free identification of extracellular vesicles by flow cytometry. *Nanomedicine* 2018;**14**:801–10. https://doi.org/10.1016/j.nano.2017.12.012
22. Bettin BA, Varga Z, Nieuwland R, van der Pol E. Standardization of extracellular vesicle concentration measurements by flow cytometry: the past, present, and future. *J Thromb Haemost* 2023;**21**:2032–44. https://doi.org/10.1016/j.jtha.2023.04.042
23. Cook S, Tang VA, Lannigan J *et al.* Quantitative flow cytometry enables end-to-end optimization of cross-platform

extracellular vesicle studies. *Cell Rep Methods* 2023;**3**:100664. https://doi.org/10.1016/j.crmeth.2023.100664
24. Ferrantelli F, Tirelli V, Barreca V, Manfredi F. Generation, characterization, and count of fluorescent extracellular vesicles. *Method Mol Biol* 2022;**2504**: 207–17. https://doi.org/10.1007/978-1-0716-2341-1_15
25. McVey MJ, Spring CM, Kuebler WM. Improved resolution in extracellular vesicle populations using 405 instead of 488 nm side scatter. *J Extracell Vesicles* 2018;**7**:1454776. https://doi.org/10.1080/20013078.2018.1454776
26. Zucker RM, Ortenzio JNR, Boyes WK. Characterization, detection, and counting of metal nanoparticles using flow cytometry. *Cytometry Pt A* 2016;**89**:169–83. https://doi.org/10.1002/cyto.a.22793
27. Libregts SFWM, Arkesteijn GJA, Németh A *et al.* Flow cytometric analysis of extracellular vesicle subsets in plasma: impact of swarm by particles of non-interest. *J Thromb Haemost* 2018;**16**: 1423–36. https://doi.org/10.1111/jth.14154
28. Van Der Pol E, Van Gemert MJC, Sturk A *et al.* Single vs. swarm detection of microparticles and exosomes by flow cytometry. *Journal of Thrombosis and Haemostasis* 2012;**10**:919–30. https://doi.org/10.1111/j.1538-7836.2012.04683.x
29. Severa M, Etna MP, Andreano E *et al.* Functional diversification of innate and inflammatory immune responses mediated by antibody fragment crystallizable activities against SARS-CoV-2. *iScience* 2024;**27**:109703. https://doi.org/10.1016/j.isci.2024.109703
30. Coscia C, Parolini I, Sanchez M *et al.* Generation, quantification, and tracing of metabolically labeled fluorescent exosomes. *Methods Mol Biol* 2016;**1448**:2017–235. https://doi: 10.1007/978-1-4939-3753-0_16
31. Gallinaro A, Borghi M, Pirillo MF *et al.* Development and preclinical evaluation of an integrase defective lentiviral vector vaccine expressing the HIVACAT T cell immunogen in mice. *Mol Ther Methods Clin Dev* 2020;**17**:418–28. https://doi.org/10.1016/j.omtm.2020.01.013
32. Morales-Kastresana A, Musich TA, Welsh JA *et al.* High-fidelity detection and sorting of nanoscale vesicles in viral disease and cancer. *J Extracell Vesicles* 2019;**8**:1597603. https://doi.org/10.1080/20013078.2019.1597603.
33. Morales-Kastresana A, Telford B, Musich TA *et al.* Labeling extracellular vesicles for nanoscale flow cytometry. *Sci Rep* 2017;**7**: 1878. https://doi.org/10.1038/s41598-017-01731-2
34. van der Pol E, Coumans FA, Grootemaat AE *et al.* Particle size distribution of exosomes and microvesicles determined by transmission electron microscopy, flow cytometry, nanoparticle tracking analysis, and resistive pulse sensing. *J Thromb Haemost* 2014;**12**:1182–92. https://doi: 10.1111/jth.12602.
35. Lee I, Choi Y, Shin DU *et al.* Small extracellular vesicles as a new class of medicines. *Pharmaceutics* 2023;**15**:325. https://doi.org/10.3390/pharmaceutics15020325
36. Welsh JA, Goberdhan DCI, O'Driscoll L, MISEV Consortium *et al.* Minimal information for studies of extracellular vesicles. (MISEV2023): from basic to advanced approaches. *J Extracell Vesicles* 2024;**13**:e12404. https://doi.org/10.1002/jev2.12404
37. van der Pol E, Welsh JA, Nieuwland R. Minimum information to report about a flow cytometry experiment on extracellular vesicles: communication from the ISTH SSC subcommittee on vascular biology. *J Thromb Haemost* 2022;**20**:245–51. https://doi.org/10.1111/jth.15540
38. Gholizadeh S, Shehata Draz M, Zarghooni M *et al.* Microfluidic approaches for isolation, detection, and characterization of extracellular vesicles: current status and future directions. *Biosensors and Bioelectronics* 2017;**91**:588–605. https://doi.org/10.1016/j.bios.2016.12.062
39. de Rond L, van der Pol E, Bloemen PR *et al.* A systematic approach to improve scatter sensitivity of a flow cytometer for detection of extracellular vesicles. *Cytometry Pt A* 2020;**97**:582–91. https://doi.org/10.1002/cyto.a.23974
40. Imanbekova M, Suarasan S, Lu Y *et al.* Recent advances in optical label-free characterization of extracellular vesicles. *Nanophotonics* 2022;**11**:2827–63. https://doi.org/10.1515/nanoph-2022-0057
41. Fortunato D, Mladenović D, Criscuoli M *et al.* Opportunities and pitfalls of fluorescent labeling methodologies for extracellular vesicle profiling on high-resolution single-particle platforms. *Int J Mol Sci* 2021;**22**:10510. https://doi.org/10.3390/ijms221910510

Biology Methods and Protocols, 2025, 10, 1–16
https://doi.org/10.1093/biomethods/bpaf019
Methods Article